The Astrophysical Journal Letters, 998:L18 (10pp), 2026 February 10 https://doi.org/10.3847/2041-8213/ae3724
© 2026. The Author(s). Published by the American Astronomical Society.
OPEN ACCESS

Bridging Scales: How Much Do Supermassive Black Holes Grow in the Suppressed Bondi Regime?

Kung-Yi Su[1,2,3], Angelo Ricarte[2,3], Priyamvada Natarajan[2,4,5], Antonio J. Porras-Valverde[4], Hyerin Cho (혜린조)[2,3], Ramesh Narayan[2,3], Claude-André Faucher-Giguère[1], Philip F. Hopkins[6], and Ben S. Prather[2]
[1] Department of Physics & Astronomy and Center for Interdisciplinary Exploration and Research in Astrophysics (CIERA), Northwestern University, 1800 Sherman Avenue, Evanston, IL 60201, USA; kungyisu@gmail.com
[2] Black Hole Initiative at Harvard University, 20 Garden Street, Cambridge, MA 02138, USA; angelo.ricarte@cfa.harvard.edu, priyamvada.natarajan@yale.edu
[3] Center for Astrophysics | Harvard & Smithsonian, 60 Garden Street, Cambridge, MA 02138, USA
[4] Department of Astronomy, Yale University, Kline Tower, 266 Whitney Avenue, New Haven, CT 06511, USA; antonio.porras@yale.edu
[5] Department of Physics, Yale University, P.O. Box 208121, New Haven, CT 06520, USA
[6] TAPIR, Mailcode 350-17, California Institute of Technology, Pasadena, CA 91125, USA
Received 2025 November 8; revised 2025 December 27; accepted 2026 January 9; published 2026 February 5

Abstract

The coevolution of supermassive black holes (SMBHs) and their host galaxies remains one of the central open questions in cosmology, rooted in the coupling between accretion, feedback, and the multiscale physics that links the event horizon to the circumgalactic medium. Here we bridge these scales by embedding a first-principles, GRMHD-informed prescription for black hole accretion and feedback—derived from multizone simulations that self-consistently connect inflows and outflows from the horizon to the Bondi radius—within cosmological magnetohydrodynamic zoom-in simulations of $\sim 10^{14} M_{\odot}$ halos. These GRMHD results predict a "suppressed Bondi" regime in which magnetic stresses and relativistic winds strongly reduce effective accretion rates in a spin-dependent manner. We find that black holes cannot grow efficiently by accretion until they exceed $\sim 10^{7} M_{\odot}$, regardless of the feedback strength. Beyond this threshold, systems bifurcate: low-spin ($\eta \sim 0.02$) black holes continue to accrete without quenching star formation, while high-spin ($\eta \gtrsim 0.3$) black holes quench effectively but become starved of further growth. Early, massive seeding partially alleviates this tension through merger-driven assembly, yet an additional cold or super-Eddington accretion mode appears essential to reproduce the observed SMBH population and the empirical black hole–galaxy scaling relations. Our results demonstrate that GRMHD-informed feedback models can account for the maintenance-mode behavior of low-luminosity active galactic nuclei like M87*, but cannot by themselves explain the full buildup of SMBH mass across cosmic time. A unified, multiregime framework is required to capture the evolving interplay between spin-dependent feedback, cold inflows, and mergers in driving coevolution.

Unified Astronomy Thesaurus concepts: Accretion (14); Active galactic nuclei (16); Bondi accretion (174); Schwarzschild radius (1435); Supermassive black holes (1663); Magnetohydrodynamical simulations (1966)

1. Introduction

The physical processes that drive gas from galactic scales into the deep potential wells of supermassive black holes (SMBHs) and then transfer the resulting energy and momentum back into the surrounding halo remain a defining uncertainty in our theory of galaxy evolution. Accretion onto SMBHs, observed as active galactic nuclei (AGN), is widely implicated as the dominant feedback channel capable of shutting down star formation and sustaining the long-lived quiescent phases of massive galaxies on the "red and dead" sequence yet the coupling mechanism is still poorly understood, especially in the most massive halos ($M \gtrsim 10^{12} M_{\odot}$) where conventional models struggle to reproduce the observed level of quenching (e.g., E. F. Bell et al. 2003; G. Kauffmann et al. 2003; D. S. Madgwick et al. 2003; I. K. Baldry et al. 2004; M. R. Blanton et al. 2005; D. Kereš et al. 2005, 2009; A. Dekel & Y. Birnboim 2006; L. Pozzetti et al. 2010; A. R. Wetzel et al. 2012; R. Feldmann & L. Mayer 2015; G. M. Voit et al. 2015).

Original content from this work may be used under the terms of the Creative Commons Attribution 4.0 licence. Any further distribution of this work must maintain attribution to the author(s) and the title of the work, journal citation and DOI.

A key empirical clue comes from the hot atmospheres of massive ellipticals and cluster cores: across the spectrum, and most starkly in X-rays, these systems harbor substantial reservoirs of hot gas (e.g., A. C. Fabian et al. 1994; J. R. Peterson & A. C. Fabian 2006; M. McDonald et al. 2011; N. Werner et al. 2013; J. Stern et al. 2019; J. Mercedes-Feliz et al. 2023). In the absence of heating, this gas should cool, condense, and ignite central star formation. Instead, the expected starbursts are largely missing (T. Tamura et al. 2001; C. P. O'Dea et al. 2008; D. A. Rafferty et al. 2008), with rare counterexamples such as the Phoenix cluster (M. McDonald et al. 2012), leaving the long-standing "cooling flow problem." The simplest inference is that star formation is being efficiently suppressed in these nuclei; alternative channels, such as stellar feedback or cosmic-ray pressure, appear insufficient on their own (K.-Y. Su et al. 2019), sharpening the case for AGN feedback as the principal regulatory agent.

Theory has been boxed in by three obstacles: complex microphysics that resist first-principles closure, limited direct observational constraints on coupling, and an extreme dynamic-range problem. Cosmological simulations have therefore adopted subgrid prescriptions for black hole accretion and feedback phenomenological closures calibrated to empirical scalings (e.g., Y. Li & G. L. Bryan 2014; D. Fiacconi et al. 2018;

D. Anglés-Alcázar et al. 2021; R. Y. Talbot et al. 2021; R. Weinberger et al. 2023) and broadly similar recipes now underpin many flagship simulation suites (e.g., D. Sijacki et al. 2015; Y. Rosas-Guevara et al. 2016; D. Anglés-Alcázar et al. 2017a; R. Weinberger et al. 2018; A. Ricarte et al. 2019; Y. Ni et al. 2022; S. Wellons et al. 2023; L. Byrne et al. 2024; A. K. Bhowmick et al. 2024). At the other end of the scale hierarchy, horizon-resolving GRMHD calculations robustly generate relativistic jets and winds (e.g., C. F. Gammie et al. 2003; A. Tchekhovskoy et al. 2011; O. Porth et al. 2019; K. Chatterjee et al. 2023), but remain too idealized to embed directly in cosmological environments. A new bridge is now emerging: multizone GRMHD frameworks that couple inflows and outflows across the full hierarchy from the event horizon to galactic scales by evolving each zone on its natural timescale and iterating to convergence, delivering a self-consistent steady state across >7 orders of magnitude (e.g., S. M. Ressler et al. 2020; A. Lalakos et al. 2022; H. Cho et al. 2023, 2024; M. Guo et al. 2023, 2024, 2025; P. F. Hopkins et al. 2024; N. Kaaz et al. 2025; P. F. Hopkins & E. R. Most 2025).

In this landscape, H. Cho et al. (2023, 2024) introduced a bidirectionally coupled multizone scheme that circumvents prohibitive horizon-scale time steps by intermittently freezing the smallest zones while allowing each annulus to respond to information propagating inward and outward, achieving a numerically converged inflow/outflow steady state. H. Cho et al. (2025) generalized the framework to spinning black holes, where jets dominate: the feedback efficiency η depends on spin a_* (e.g., $\eta \sim 0.3$ for $a_* = 0.9$ and $\eta \sim 0.02$ for $a_* = 0$) while remaining insensitive to the Bondi radius. The first closed loop from galaxy initial conditions into multizone GRMHD and back was completed in H. Cho et al. (2024) and K.-Y. Su et al. (2025b), showing that even minimal efficiencies can stabilize already-assembled $z = 0$ SMBHs, and that for $\eta \gtrsim 0.15$ the accretion rates can be regulated to those inferred for M87* and Sgr A* by the Event Horizon Telescope (Event Horizon Telescope Collaboration et al. 2021; Event Horizon Telescope Collaboration et al. 2022).

The open question, and the focus of this work, is whether GRMHD-informed low-Eddington feedback can simultaneously permit SMBH growth *and* quench star formation during assembly. We implement the multizone GRMHD-calibrated accretion suppression and spin-dependent feedback efficiencies in a cosmological zoom-in simulation of a halo with a $z = 0$ mass of $\sim 10^{14} M_\odot$ surveying spin states and seeding prescriptions to map the conditions under which the SMBH can grow while quenching its massive host, and to identify when this accretion mode dominates the SMBH's overall mass growth. We note that the question described above is generic to massive cluster ellipticals and SMBHs, so we do not intend to exactly match M87 in our zoom-in simulations.

2. Methodology

We perform cosmological zoom-in simulations of a halo with a $z = 0$ mass (M_{200c}) of $1.1 \times 10^{14} M_\odot$ using the GIZMO code[7] (P. F. Hopkins 2015). The entire zoom-in region has a radius of ~ 10 comoving Mpc h^{-1}. We run GIZMO in meshless finite-mass mode, a Lagrangian mesh-free Godunov hydrodynamics scheme that combines the strengths of grid-based and smoothed-particle hydrodynamics. Numerical algorithms and code tests, including hydrodynamics, self-gravity, and magnetohydrodynamics, are described in P. F. Hopkins (2015, 2016) and P. F. Hopkins & M. J. Raives (2016).

All simulations use the FIRE-2 framework for gas cooling, the interstellar medium (ISM), star formation, and stellar feedback (see Appendix A.1), with finest gas mass resolution $\sim 4 \times 10^5 M_\odot h^{-1}$ and jet mass resolution $\sim 5 \times 10^4 M_\odot h^{-1}$. The methodology and its numerical tests are described in detail in P. F. Hopkins et al. (2018a); we summarize only key elements here. FIRE-2 follows radiative cooling from 10 to 10^{10} K, and stellar feedback from supernovae, stellar winds, and radiation. Star formation uses a sink-particle prescription restricted to gas that is dense, molecular, self-shielding, and locally self-gravitating.

Black hole accretion is modeled based on the Bondi prescription,

$$\dot{M}_{\rm Bondi} = \frac{4\pi \rho G^2 M_{\rm BH}^2}{(c_s^2 + \Delta v^2)^{3/2}}, \tag{1}$$

where ρ is the local gas density, c_s is the mean sound speed, and Δv is the mean relative velocity near the black hole. These quantities are evaluated by averaging within a kernel enclosing 96 effective neighbors, subject to a minimum radius of 50 comoving pc h^{-1} (see Appendix A.2).

The actual black hole accretion rate is scaled by the Bondi rate by a prefactor $f_{\rm mass,acc}$, following the multizone GRMHD-informed model of H. Cho et al. (2024, 2025):

$$\begin{aligned} \dot{M}_{\rm BH} &= f_{\rm mass,acc}\, \dot{M}_{\rm Bondi} \\ f_{\rm mass,acc} &= \kappa_{\rm cho} \equiv \left(\frac{r_B}{6 r_g}\right)^{-1/2} \\ &= \left(\frac{6(c_{s,\infty}^2 + \Delta v^2)}{c^2}\right)^{1/2}, \end{aligned} \tag{2}$$

where $r_B \equiv G M_{\rm BH}/(c_{s,\infty}^2 + \Delta v^2)$ is the Bondi radius, $r_g \equiv G M_{\rm BH}\, c^{-2}$ is the gravitational radius, and $\kappa_{\rm cho}$ is the suppression factor obtained in H. Cho et al. (2024, 2025).

AGN feedback is treated as an isotropic wind that predominantly carries kinetic energy using the particle spawning method. The mass and energy fluxes of the outflow are given by

$$\begin{aligned} \dot{M}_{\rm wind} &= f_{\rm mass,wind}\, \dot{M}_{\rm Bondi}. \\ \dot{E}_{\rm wind} &= \eta \dot{M}_{\rm BH} c^2 = \frac{1}{2} \dot{M}_{\rm wind} V_{\rm wind}^2, \end{aligned} \tag{3}$$

where $f_{\rm mass,wind} = 1 - \kappa_{\rm cho}$ for runs with feedback and η is the efficiency of kinetic feedback. The corresponding wind velocity is given by

$$V_{\rm wind} = \left(\frac{2\eta f_{\rm mass,acc}}{f_{\rm mass,wind}}\right)^{1/2} c = \left(\frac{2\eta \kappa_{\rm cho}}{1 - \kappa_{\rm cho}}\right)^{1/2} c. \tag{4}$$

Details of the numerical implementation are given in Appendix A.3. Limitations of the model, such as neglected geometric effects, are discussed further in K.-Y. Su et al. (2025b) and improvements are deferred to future work.

[7] A public version of GIZMO is available at http://www.tapir.caltech.edu/~phopkins/Site/GIZMO.html

Table 1
Parameter Choices and Initial Conditions in Our Simulations

	Model	Numerical Details		Seeding Parameter		Feedback Parameter				
		$z_{\rm final}$	$m_{\rm wind}$ ($M_\odot\,h^{-1}$)	$M_{\rm star}$ ($M_\odot\,h^{-1}$)	$M_{\rm BH}$ ($M_\odot\,h^{-1}$)	$T_{\rm wind}$ (K)	$B_{\rm wind}$ (G)	$f_{\rm mass,acc}$	$f_{\rm mass,wind}$	$\eta_{\rm Kin}$
Fiducial Seeding										
A/B	Fiducial–$\eta = 0.$	1	⋯	3×10^{10}	3.5×10^{7}	⋯	⋯	$\kappa_{\rm Cho}$	$1 - \kappa_{\rm Cho}$	0
C1	Fiducial–$\eta = 0.02$	1	5×10^{4}	3×10^{10}	3.5×10^{7}	10^{7}	10^{-4}	$\kappa_{\rm Cho}$	$1 - \kappa_{\rm Cho}$	0.02
C2	Fiducial–$\eta = 0.3$	1	5×10^{4}	3×10^{10}	3.5×10^{7}	10^{7}	10^{-4}	$\kappa_{\rm Cho}$	$1 - \kappa_{\rm Cho}$	0.3
C3	Fiducial–$\eta = 1$	1	5×10^{4}	3×10^{10}	3.5×10^{7}	10^{7}	10^{-4}	$\kappa_{\rm Cho}$	$1 - \kappa_{\rm Cho}$	1
Light Seeding										
B	Light–$\eta = 0.$	1	⋯	3×10^{10}	3.5×10^{6}	⋯	⋯	$\kappa_{\rm Cho}$	$1 - \kappa_{\rm Cho}$	0
C1	Light–$\eta = 0.02$	1	5×10^{4}	3×10^{10}	3.5×10^{6}	10^{7}	10^{-4}	$\kappa_{\rm Cho}$	$1 - \kappa_{\rm Cho}$	0.02
C3	Light–$\eta = 1$	1	5×10^{4}	3×10^{10}	3.5×10^{6}	10^{7}	10^{-4}	$\kappa_{\rm Cho}$	$1 - \kappa_{\rm Cho}$	1
Early Seeding										
A	Early–NoAcc/NoFB	1	⋯	3×10^{9}	3.5×10^{7}	⋯	⋯	0	0	0
B	Early–$\eta = 0.$	1	⋯	3×10^{9}	3.5×10^{7}	⋯	⋯	$\kappa_{\rm Cho}$	$1 - \kappa_{\rm Cho}$	0
C1	Early–$\eta = 0.3$	1	5×10^{4}	3×10^{9}	3.5×10^{7}	10^{7}	10^{-4}	$\kappa_{\rm Cho}$	$1 - \kappa_{\rm Cho}$	0.3
C3	Early–$\eta = 1$	1	5×10^{4}	3×10^{9}	3.5×10^{7}	10^{7}	10^{-4}	$\kappa_{\rm Cho}$	$1 - \kappa_{\rm Cho}$	1

Note. List of the runs: (1) Model name. (2) $z_{\rm final}$: Final redshift for the run. (3) $m_{\rm wind}$: Mass resolution of the spawned AGN wind particles. (4) $M_{\rm star}$: Stellar mass to initiate seeding. (5) $M_{\rm BH}$: Seed black hole mass. (6,7) $T_{\rm wind}$ and $B_{\rm wind}$. (8,9) $f_{\rm mass,acc}$/$f_{\rm mass,wind}$: The accretion rate and the wind mass flux with respect to Bondi. (10) $\eta_{\rm Kin}$: The kinetic AGN feedback efficiencies. Note that $\eta_{\rm Kin} = 0.02$ corresponds to a spin of $a_* = 0$, while $\eta_{\rm Kin} = 0.3$ corresponds to $a_* = 0.9$.

We perform an on-the-fly friend-of-friends search over all particles and seed a fixed-mass black hole once the stellar mass reaches a specified threshold (V. Springel et al. 2001). We consider three seeding scenarios: (1) *fiducial seeding*—when the stellar mass reaches $3 \times 10^{10} M_\odot\,h^{-1}$, we seed a $3.5 \times 10^{7} M_\odot\,h^{-1}$ black hole; (2) *light seeding*—at the same threshold, we seed a $3.5 \times 10^{6} M_\odot\,h^{-1}$ black hole; and (3) *early seeding*—when the stellar mass reaches $3 \times 10^{9} M_\odot\,h^{-1}$, we seed a $3.5 \times 10^{7} M_\odot\,h^{-1}$ black hole. The first seeding events occur at $z = 4.5$, 4.5, and 7.2, respectively. Once seeded, the black hole is gradually migrated toward the potential minimum via an additional artificial acceleration toward the most bound collisionless particle in its interaction kernel each time step (S. Wellons et al. 2023).

For each seeding model, we run a subset of five simulations: (i) Run A—no or minimal accretion and no feedback; (ii) Run B—black hole accretion suppressed relative to the Bondi rate ($f_{\rm mass,acc} = \kappa_{\rm Cho}$) but no AGN feedback; and (iii) Runs C1, C2, and C3—suppressed Bondi accretion with three AGN feedback efficiencies, $\eta = 0.02$, 0.3, 1. The first two values span the low to high efficiencies predicted by multizone GRMHD simulations (H. Cho et al. 2025) for $a_* = 0$ and $a_* = 0.9$. The third, $\eta = 1$, corresponds to $a_* = 0.9$ and steady prograde rotation (e.g., H. Cho & R. Narayan 2025). Run parameters are summarized in Table 1. Note that we did not include a standard, nonsuppressed Bondi accretion run with no feedback. Instead, we use the suppressed Bondi run with no feedback as the reference point. The reason is that, as we will later show, except for the light-seed case, even with suppressed Bondi accretion, the black hole quickly undergoes runaway growth, and an unsuppressed Bondi accretion run would only be worse (tests in K.-Y. Su et al. 2025b). For the light-seed case, if a standard Bondi no-feedback run were included, the likely outcome should be similar to the fiducial seeding case with suppressed Bondi accretion. The reason is that removing the suppression factor, which was $\lesssim$0.01, compensates the $M_{\rm BH}^2$ factor even in the light-seed case, where $M_{\rm BH}$ is lowered by 1 order of magnitude.

3. Results

3.1. Properties of the Stellar and Black Hole Masses

Figure 1 presents the statistical properties of the black hole population, the host galaxy stellar masses, and corresponding halo masses in the simulations, shown in both the stellar mass–halo mass relation and the black hole mass–stellar mass relation. For simplicity, we plot the properties of all subhalos where the Lagrangian region is contaminated by <10% low-resolution elements, evaluated across all times.[8] Different columns correspond to different seeding models.

For black hole seeds with $M_{\rm BH} < 10^{7} M_\odot$ (light seeding), both accretion and the resulting feedback are weak. As a result, the black holes fail to grow, and the star formation in galaxies also remains unquenched. This negligible growth persists even in the absence of feedback ($\eta = 0$). Consequently, the stellar mass produced above $M_{\rm Halo} \gtrsim 10^{12} M_\odot$ consistently exceeds empirical values, due to the weak AGN feedback.

In the fiducial-seeding case, both accretion and feedback are stronger, and the feedback efficiency critically influences black hole growth. Without feedback, the black hole overgrows, while with efficiencies matching the $a_* = 0$ result ($\eta = 0.02$), it grows only moderately. For efficiencies corresponding to the high spinning case studied ($\eta \geqslant 0.3$), the black hole fails to grow through accretion. Star formation is quenched only in this high-efficiency regime.

We therefore encounter an intriguing dilemma, in which the black hole falls into one of two possible cases.

[8] Note that the cutoff is to select halos in the zoom-in region, and most halos that fulfill that cut have a much lower contamination rate, and changing the cutoff should not change the result.

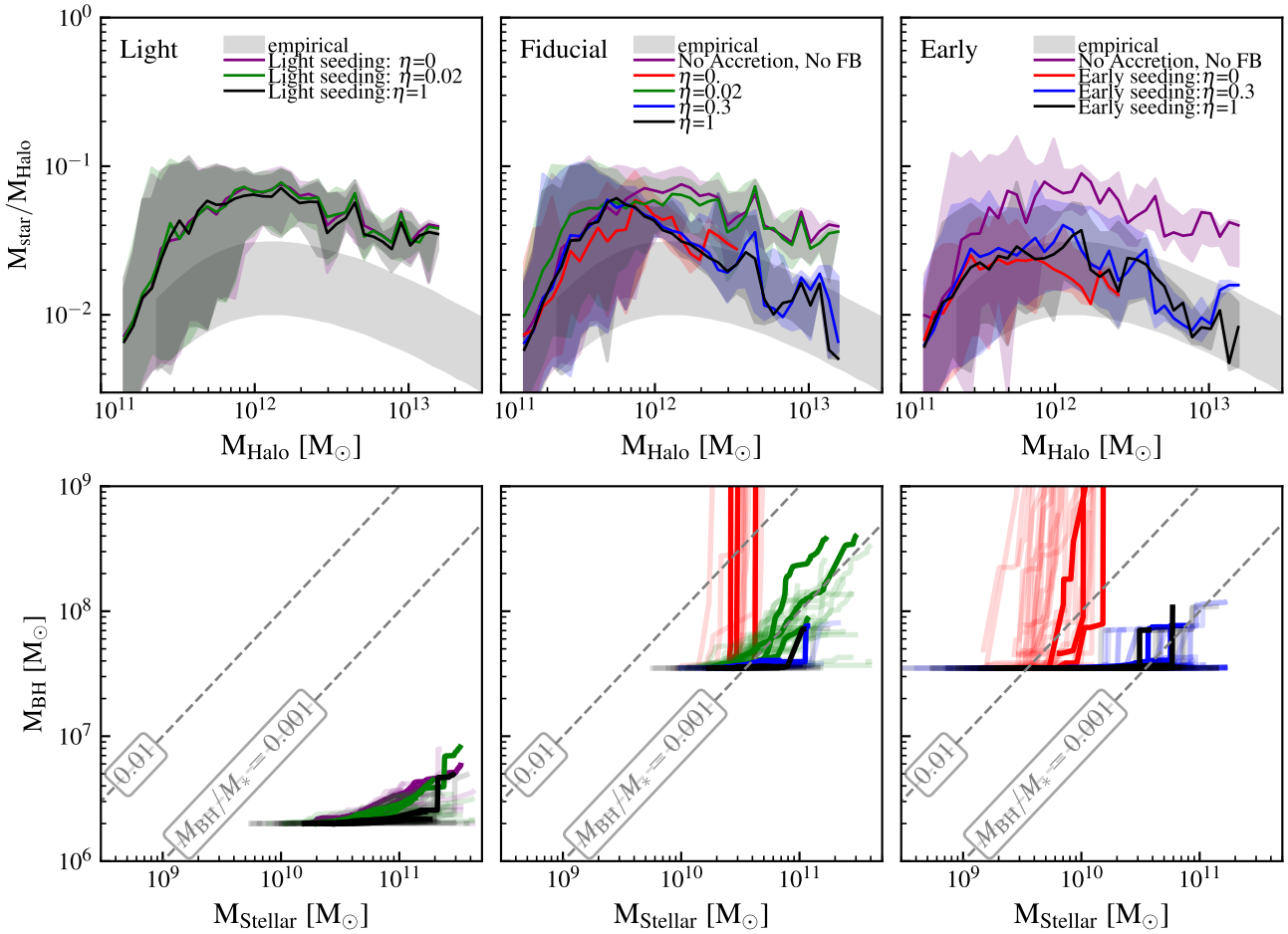

Figure 1. Stellar mass–halo mass relation (top) and black hole mass–stellar mass relation (bottom) for the light-seeding (left), fiducial-seeding (center), and early-seeding (right) models. The shaded region, which represents the empirical relation at $z = 1$ (P. S. Behroozi et al. 2010), should be treated as a guide for the eye, as we overplot results from all redshifts. For seed black holes with $M_{\rm BH} < 10^7 M_\odot$, the black hole does not grow, and the galaxy is not quenched, regardless of feedback efficiencies, resulting in excess stellar mass above $M_{\rm Halo} \gtrsim 10^{12} M_\odot$. In the fiducial seeding case, the black hole overgrows without feedback, grows moderately when the efficiency matches $a_* = 0$ result, and fails to accrete when the efficiency corresponds to maximum spin ($\eta \gtrsim 0.3$); star formation is also quenched in this high-efficiency case. With early massive seeding, black holes still do not grow through accretion for $\eta \gtrsim 0.3$, but growth through mergers can reproduce the observed local black hole–stellar mass relation. Galaxy quenching is also more efficient, yielding better agreement with the local stellar mass–halo mass relation.

1. *Nonspinning black hole ($a_* = 0$).* The feedback efficiency is low. The black hole accretes without quenching star formation.
2. *Higher black hole spin ($a_* \gtrsim 0.9$).* The feedback efficiency is high. The black hole quenches star formation but fails to grow through accretion.

With early massive seeding, a comparable mass black hole begins accreting and providing feedback earlier at a higher redshift. As before, black holes are seen to overgrow compared to the local relation in the absence of feedback, but fail to grow through accretion for $\eta \geqslant 0.3$. The difference is that in the early seeding case, although the black hole still does not accrete substantially at early times, growth through mergers that is expected to dominate at these epochs may be sufficient to reproduce the observed local black hole–stellar mass relation (see Section 4.1). As we can see from Figure 1, most of the growth occurs in vertical jumps, which correspond to merger events. The earlier presence of a more massive black hole at fixed halo mass also makes the feedback relatively stronger and allows it to operate at an earlier stage. This causes quenching to occur earlier and more efficiently, yielding better agreement with the local stellar–halo mass relation.

In addition to the statistical properties, a similar conclusion can be drawn from Figure 2, which shows the stellar mass, star formation rate, and black hole accretion rate of the most massive progenitor as a function of time. In addition to the accretion rate of the specific black hole, the shaded region indicates the 16th–84th percentile distribution of the black hole population.

In order to suppress star formation in the most massive progenitor, the black hole must exceed $3 \times 10^7 M_\odot h^{-1}$ and have a feedback efficiency $\geqslant 0.3$ (corresponding to a spin $a_* \gtrsim 0.9$). Otherwise, the feedback remains too weak to be impactful.

Similarly, suppressing black hole growth requires a feedback efficiency of $\eta \geqslant 0.3$ (or $a_* \gtrsim 0.9$) to produce a visible effect.

3.2. Suppression of Accretion

The dilemma manifests itself as the system falling into one of two regimes: the black hole either accretes without quenching or quenches but does not grow. This outcome arises from the strong suppression of the accretion rate relative to the Bondi rate. Figure 3 shows the time evolution of κ, together with the corresponding effective temperature around

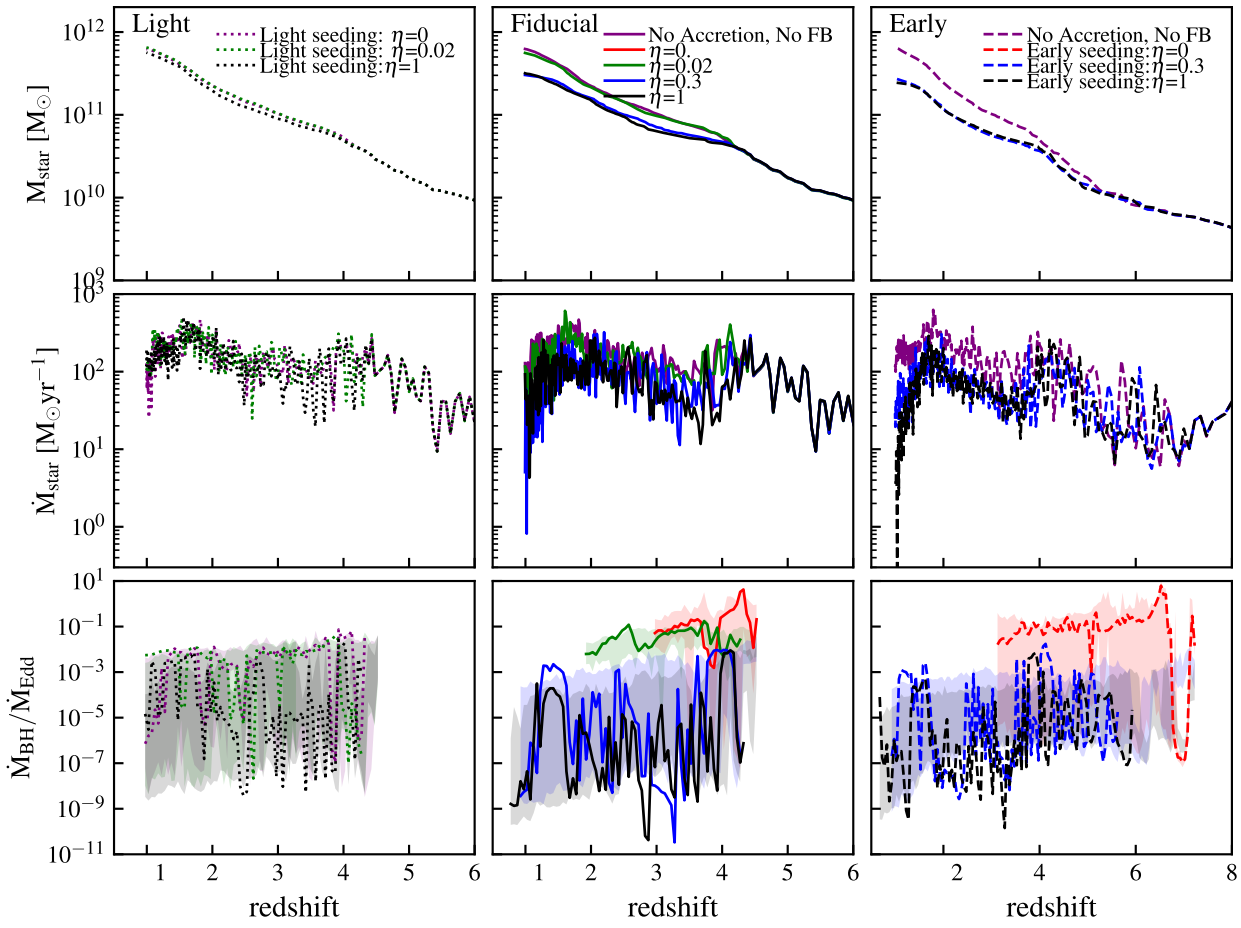

Figure 2. The stellar mass (top), star formation rate (middle), and black hole accretion rate (bottom) of the most massive progenitor in the light-seeding (left), fiducial-seeding (center), and early-seeding (right) models. The shaded region shows the 16th–84th percentile range of the accretion rate across all black holes in the run at each time. Black holes with $M_{\rm BH} \lesssim 10^7 M_\odot$ do not impact the star formation rate regardless of feedback efficiency. For $M_{\rm BH} \gtrsim 3 \times 10^7 M_\odot$, feedback efficiencies $\eta \gtrsim 0.3$ ($a_* \gtrsim 0.9$) lead to efficient quenching of star formation, while efficiencies $\eta \lesssim 0.02$ remain ineffective. A feedback efficiency $\gtrsim$0.3 always suppresses black hole accretion, regardless of black hole mass.

the black hole and the implied Bondi radius relative to the gravitational radius (Equation (2)). The shaded regions denote the 16th–84th percentile range as well as the full distribution at each time. Note that the effective temperature is defined as the average $T_{\rm eff} = m(c_s^2 + \Delta v^2)/\gamma k$ within the black hole kernel, where m is the mean particle mass.

Regardless of the seeding model, higher feedback efficiency consistently produces hotter gas near the black hole and a larger separation between r_B and r_g, which corresponds to a larger κ. In all cases, κ lies within 10^{-3}–10^{-2}, with a median value of 1–3 $\times$ 10^{-3}. This represents a dramatic suppression and is the primary reason why it is difficult for black holes to grow while simultaneously quenching star formation.

We also find that more massive black holes, arising from either earlier or heavier seeding, produce broader distributions of κ, temperature, and r_B/r_g. This occurs because a more massive black hole can drive stronger episodes of feedback, temporarily heating the surrounding gas, while also encountering denser gas due to the deeper potential well. The net effect is that, despite the broader distribution, the median κ for more massive black holes—whether due to earlier or more massive seeding—is lower, reflecting a lower ambient temperature. For the early-seeding case, the less stringent seeding criteria also place black holes in many more low-mass halos, which impacts the temperature statistics.

3.3. Gas Morphology

Figure 4 shows the gas temperature and density morphology at $z \sim 1.2$ for the seven runs with nonzero feedback efficiency, along with one run without feedback for reference. Because the timing of individual AGN feedback episodes varies from run to run, we selected snapshots that best illustrate the differences. Runs with higher feedback efficiency ($\eta \geqslant 0.3$) inject feedback with a higher specific energy, producing stronger episodes that propagate to larger radii. This is evident in both the higher temperatures and the reduced densities that extend to large scales.

4. Discussion and Conclusions

4.1. Paths Out of the Dilemma

In Section 3, we showed that if multizone GRMHD-informed magnetically suppressed black hole accretion and AGN feedback are assumed to be the only modes of growth and feedback, the system faces the following dilemma: the black hole either accretes without quenching star formation, as in the case of lower feedback efficiency or a nonspinning ($a_* = 0$) black hole, or it quenches but fails to grow through accretion, as in the case of higher feedback efficiency or rapidly spinning black holes ($a_* \gtrsim 0.9$).

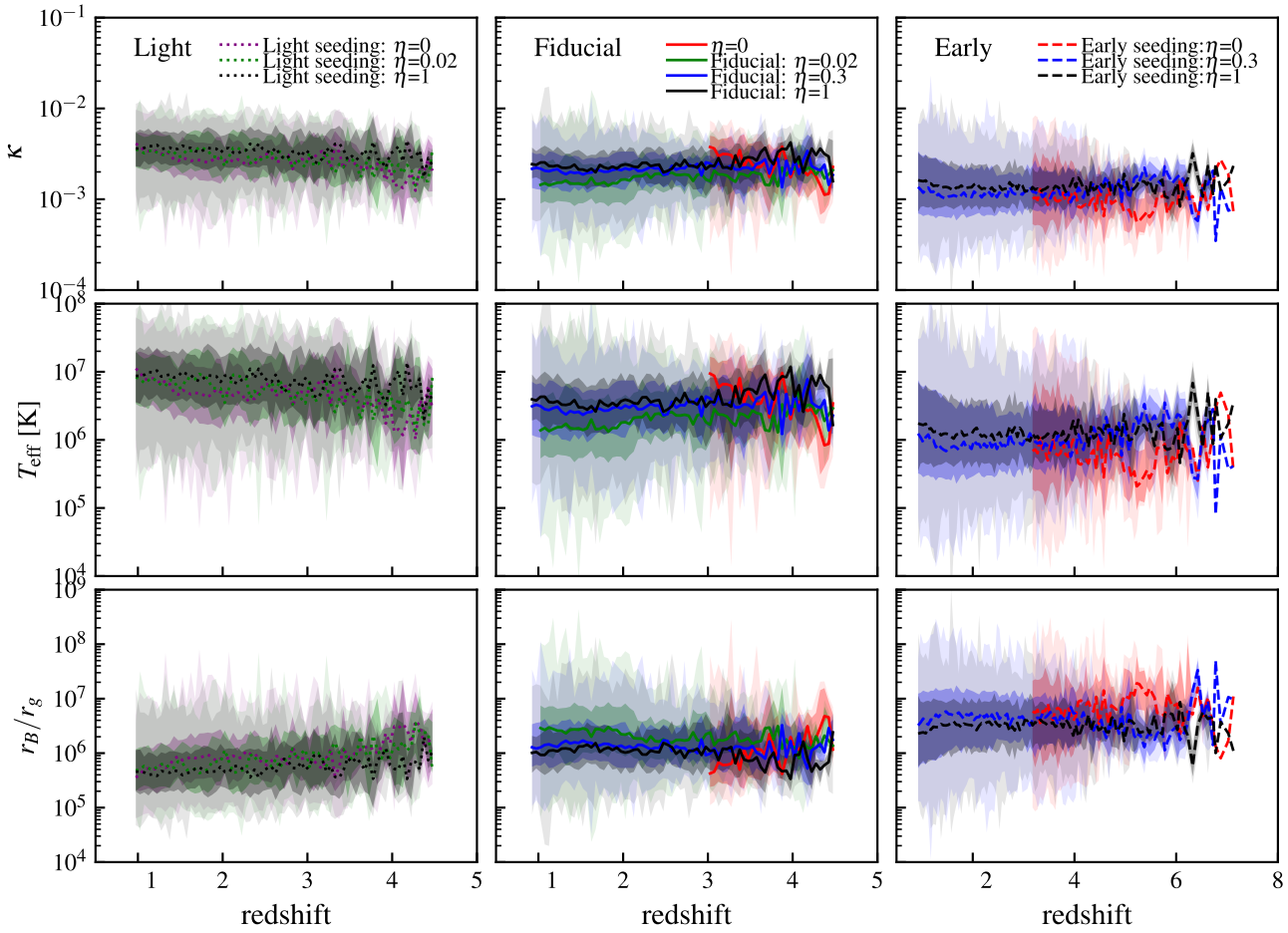

Figure 3. The evolution of accretion suppression (top, $\kappa \equiv \dot{M}_{\rm BH}/\dot{M}_{\rm Bondi}$), the corresponding gas temperature (middle), and the Bondi radius (bottom) for the light-seeding (left), fiducial-seeding (center), and early-seeding (right) models. The shaded regions show the full distribution and the 16th–84th percentile range. In all cases, the suppression of black hole accretion relative to the Bondi rate falls within $\sim 10^{-3}$–10^{-2}. Higher feedback efficiency produces hotter gas around the black hole and thus larger κ. More massive black holes, resulting from earlier or more massive seeding, lead to broader distributions of κ, temperature, and r_B/r_g, and systematically lower average κ and temperatures.

Moreover, the black hole does not grow through this mode of accretion before reaching $\sim 10^7 M_\odot\, h^{-1}$, even in the absence of feedback.

We also noted that this dilemma originates from the highly suppressed accretion rate. Yet, in the Universe, we clearly observe black holes more massive than $10^8 M_\odot$ as well as quenched galaxies. To reconcile this dilemma with the observations, there are several possible ways forward.

1. *A separate cold or super-Eddington accretion mode*. The multizone GRMHD simulations are designed to mimic an SMBH in a hot, sub-Eddington environment, where accretion is strongly suppressed by magnetic fields. However, the mode of black hole growth informed by these simulations may not be the only relevant scenario —particularly at earlier stages, before the black hole has grown into an SMBH and before the host galaxy has evolved into a massive cluster elliptical. A separate treatment of cold gas accretion, such as via gravitational torque models (P. F. Hopkins & E. Quataert 2010; D. Anglés-Alcázar et al. 2017a, 2017b; L. Byrne et al. 2023; A. J. Porras-Valverde et al. 2025b) or chaotic cold accretion models (M. Gaspari et al. 2013), may be required to explain black hole growth and feedback in the supermassive regime, and appears essential for describing black hole growth prior to reaching $\sim 10^7 M_\odot\, h^{-1}$. In such models, a larger fraction of the available gas can be funneled onto the black hole (see also how gravitational instabilities contribute to black hole mass assembly in Dark Sage; A. J. Porras-Valverde et al. 2025b). This pathway is also consistent with observations of cold gas around black holes (e.g., M. D. Gorski & E. Murchikova 2025), as well as with previous studies concluding that black holes do not gain significant mass during the ADAF phase, and that most of their growth must have occurred during an earlier, radiatively efficient, super-Eddington stage (P. F. Hopkins et al. 2006a, 2006b). Part of this issue is explored in our separate work using semianalytic models in A. J. Porras–Valverde et al. 2025a.
2. *Spin dependence of feedback*. We demonstrate that for a feedback efficiency of $\eta \sim 0.02$, mimicking zero black hole spin, the black hole grows but does not quench, while for $\eta \geqslant 0.3$, corresponding to the rapidly spinning case of the multizone GRMHD simulations, the opposite occurs. A possible way forward is to track black hole spin by following the angular momentum of the accreted gas, and including spin-down due to feedback. For example, incoherent accretion could keep spins low

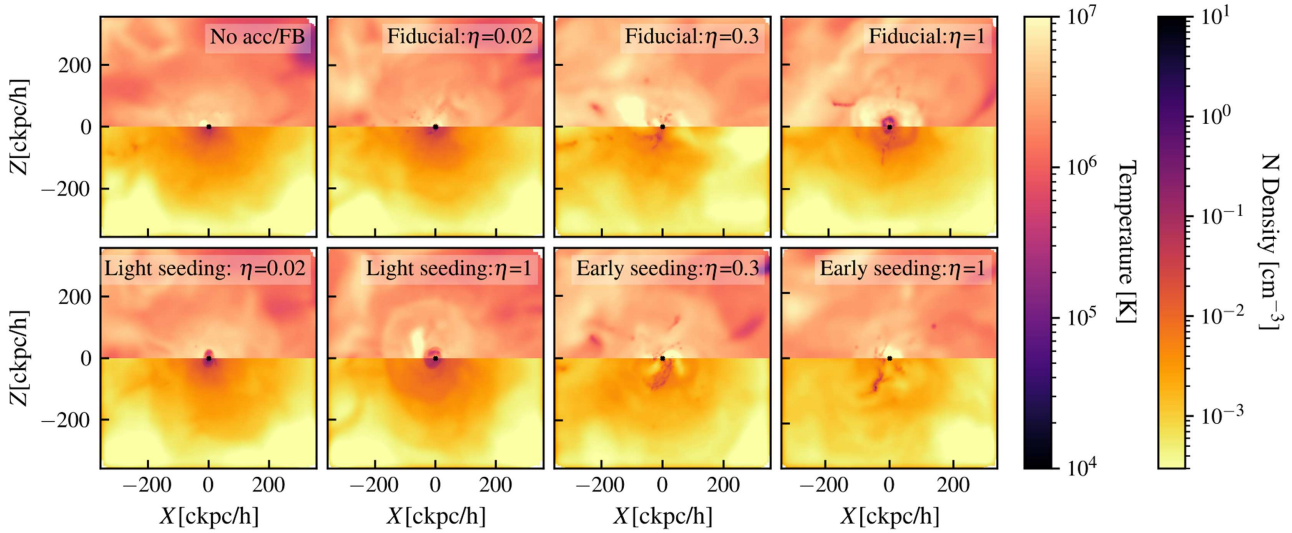

Figure 4. The gas temperature (upper half) and density (lower half) morphology at $z \sim 1.2$ for seven runs with AGN feedback and one without. For $\eta = 0.02$, AGN feedback produces minimal changes to the gas morphology, while efficiencies $\eta \gtrsim 0.3$ generate visible outflows extending to large radii.

during periods of efficient accretion, while black hole–black hole mergers could provide larger spins at later times (A. Ricarte et al. 2025). This might possibly allow a balance between the two extremes: during low-spin episodes, the black hole can grow, while during high-spin episodes it can produce strong feedback and quench star formation.

3. *Collimated feedback*. Although we model our feedback as isotropic regardless of black hole spin, jet feedback from a rapidly spinning black hole remains collimated at the Bondi radius (H. Cho et al. 2025). When the outflow geometry is properly accounted for, such collimated feedback may be less effective at suppressing accretion near the black hole than the isotropic case with identical total feedback efficiency. As a result, it can sustain a more stable accretion flow while depositing energy at larger radii, balancing black hole growth and galaxy quenching. This will be left for future study and is further discussed in Appendix B.3.
4. *Abundant early massive black holes boost merger-driven growth*. We partially demonstrate this with runs adopting an earlier, more massive seeding criterion: when a halo's stellar mass first reaches $3 \times 10^9 M_\odot h^{-1}$, we initiate a black hole with $M_{\rm BH}/M_\star \sim 1/100$ (also see e.g., P. Kroupa et al. 2020; A. K. Bhowmick et al. 2025, 2026). In this case, although the black holes still do not accrete for high feedback efficiencies ($\eta \gtrsim 0.3$), the less stringent seeding threshold substantially increases the number of black holes and hence the merger rate. This enhanced merger activity is sufficient to evolve the system from $M_{\rm BH}/M_\star \sim 1/100$ to the local relation of $\sim 1/1000$. These runs agree best with the local black hole–stellar mass relation as well as with empirical stellar mass–halo mass relations. The latter is due to the presence of a more massive black hole at earlier cosmic epochs, which provides stronger and earlier feedback.

Either one or a combination of the four paths outlined above should be sufficient to reconcile the discrepancy between the dilemma and the observational evidence. We emphasize, however, that the latter three paths can only remedy the situation once a black hole has already reached a few times $10^7 M_\odot$, while a separate treatment of cold or super-Eddington accretion is essential for growing the black hole to that mass scale in the first place.

4.2. Summary

1. *Bridging scales*. We present a unified framework that connects the physics of black hole accretion and feedback across the full hierarchy of scales—from the event horizon to the galactic environment—by embedding a GRMHD-informed, multizone accretion and feedback model (H. Cho et al. 2023, 2024, 2025) within cosmological magnetohydrodynamic zoom-in simulations.
2. *First-principles modeling*. This approach links relativistic inflows and outflows to galaxy-scale dynamics, enabling a self-consistent exploration of how SMBHs grow and regulate their hosts in the suppressed Bondi regime.
3. *Key finding—suppressed growth*. Multizone GRMHD-informed feedback yields accretion rates far lower than predicted by traditional Bondi models, effectively stalling SMBH growth until black holes exceed masses of $\sim 10^7 M_\odot$ even without any feedback.
4. *Bifurcation in evolutionary outcomes*. For black holes above $\sim 10^7 M_\odot$, the system falls into the following two cases under the multizone GRMHD-informed feedback and accretion model.
   a. *Low-spin systems ($a_* \sim 0$ or $\eta \sim 0.02$)*. Continue to accrete at low rates, without quenching star formation.
   b. *High-spin systems ($a_* = 0.9$ or $\eta \gtrsim 0.3$)*. Quench star formation efficiently but rapidly deplete their gas supply, limiting further black hole growth.
5. *Physical implications*. This spin-dependent bifurcation explains the observed coexistence of massive quenched galaxies with dormant black holes and star-forming systems with modestly growing nuclei.
6. *Need for additional channels*. GRMHD-regulated accretion alone cannot account for the full observed SMBH

mass spectrum. Additional growth mechanisms—major mergers, cold inflows, or brief super-Eddington episodes—are required, particularly at high redshift. Our results highlight the need for an evolving, multiregime model of SMBH growth that captures the interplay between spin, feedback, and environment, offering a physically grounded framework for coevolution across cosmic time.

Acknowledgments

We thank the referee for the very helpful comments. K.S., P. N., H.C., R.N., and B.P. were partially supported by the black hole Initiative at Harvard University, which is funded by the Gordon and Betty Moore Foundation grant 8273, and the John Templeton Foundation grant 61497. The opinions expressed in this publication are those of the authors and do not necessarily reflect the views of the Moore or Templeton Foundation. CAFG was supported by NSF through grants AST-2108230 and AST-2307327; by NASA through grants 80NSSC22K1124, 21-ATP21-0036, and 23-ATP23-0008; by STScI through grant JWST-AR-03252.001-A; and by BSF grant #2024262. Support for P.F.H. was provided by NSF Research grants 1911233, 20009234, and 2108318, NSF CAREER grant 1455342, and NASA grants 80NSSC18K0562 and HST-AR-15800. This work was performed in part at Aspen Center for Physics, which is supported by National Science Foundation grant PHY-2210452. The simulations are done on Frontera with allocation AST22010, and Bridges-2 with Access allocations TG-PHY220027 and TGPHY220047. This research also used resources provided to B.P. by the Los Alamos National Laboratory Institutional Computing Program, which is supported by the U.S. Department of Energy National Nuclear Security Administration under contract No. 89233218 CNA000001. We thank FIRE and LtU collaboration for useful discussions.

Appendix A
Numerical Details

A.1. Stellar Physics

Our simulations utilize the Feedback In Realistic Environments (FIRE-2) framework for modeling the ISM, star formation, and stellar feedback, as described in detail in P. F. Hopkins et al. (2018a), which also presents extensive numerical validations. Radiative cooling is followed from 10 to 10^{10} K, accounting for a wide range of processes including photoelectric and photoionization heating, Compton and collisional cooling, fine-structure emission, recombination, and both atomic and molecular cooling channels. The simulations implement a time-dependent but uniform cosmic UV/X-ray background following C.-A. Faucher-Giguère et al. (2009).

Star formation occurs in gas that is dense ($n > 1000\,\mathrm{cm}^{-3}$), molecular, self-shielding, and locally self-gravitating, implemented through a sink-particle scheme (P. F. Hopkins et al. 2013). Once formed, star particles represent entire stellar populations with metallicities inherited from their progenitor gas particles. Stellar feedback rates—including supernovae, stellar winds, and radiation—are computed using initial mass function-averaged outputs from STARBURST99 (C. Leitherer et al. 1999), assuming a P. Kroupa (2002) initial mass function.

The feedback model includes several key processes: (1) radiative feedback from photoionization, photoelectric heating, and radiation pressure across five wavelength bands (ionizing, far-ultraviolet (FUV), near-ultraviolet (NUV), optical–near-infrared (NIR), and IR); (2) stellar winds from OB and asymptotic giant branch (AGB) stars, which contribute continuous injection of mass, metals, momentum, and thermal energy; and (3) both Type Ia and Type II supernovae, including prompt and delayed events, with ejecta and energetics prescribed from tabulated stellar evolution models. Magnetohydrodynamics is included in all runs.

A.2. Black Hole Accretion and the Density and Temperature Estimate within

The characteristic temperature and density computed in the multizone GRMHD simulation is the large-scale temperature and density, t_∞ and n_∞. These are the factors that determine the accretion rate and the suppression factor in Equations (1) and (2). However, in both the cosmological zoom-in simulations and the multizone GRMHD simulations that use a galaxy simulation as the outer boundary condition (H. Cho et al. 2024), the temperature is not necessarily constant at large radius, and the characteristic temperature in these cases should be the temperature near the Bondi radius.

To evaluate the gas density used in the Bondi accretion rate and the suppression factor $\kappa_{\rm Cho}$ in the zoom-in simulation, we compute kernel-weighted averages of the density and temperature within a radius r_d. This radius is defined as enclosing 96 kernel-weighted neighbors, with a minimum enforced value of $r_d > 50\ \mathrm{pc}\,h^{-1}$. In the light-seeding runs, we instead adopt a directly averaged density over the same radius; however, we find this has a negligible impact on the resulting black hole accretion, in part because these black holes do not accrete significantly under the assumed seeding conditions.

Spawned gas particles are explicitly excluded from the density and temperature calculations to prevent noise in the estimated local quantities, and they are also not allowed to be accreted by the black hole.

Although the radius reached by the neighborhood search is not necessarily comparable to the Bondi radius, H. Cho et al. (2024; see their Figure 5) show that the gas density and temperature profiles are relatively flat beyond the Bondi radius over the range 10^5–$10^8\ r_g$ (corresponding to ∼30 pc–10 kpc). For simplicity, we therefore adopt the density and temperature values measured directly in the simulation without applying any rescaling. A more detailed analysis of the implications of this choice is provided in K.-Y. Su et al. (2025b).

We also note that the Bondi accretion formula used in Equation (1) for suppressed Bondi accretion is the canonical Bondi–Hoyle–Lyttleton expression, which accounts for the relative velocity between the gas and the black hole. However, the corresponding velocity dependence is not verified by multizone GRMHD simulations. Velocity dispersion is also not accounted for in the expression. We apply the same formula to all gas phases, including low-temperature gas, assuming the functional dependence is universally applicable, although multizone GRMHD simulations have only tested it in the regime of $T_\infty \gtrsim 10^6$ K. The broader applicability will be left for future multizone GRMHD work. The expression also asymptotes to 4 times the adiabatic Bondi accretion rate assuming $\gamma = 5/3$, and is numerically closer to the case assuming $\gamma = 1$, given that galaxy simulations are

nonadiabatic and such an expression behaves better in the limit where the sound speed is low. We emphasize that uncertainties in the overall normalization—by a factor of a few—arising from either density estimation or the choice of Bondi expression, which apply simultaneously to both the black hole accretion rate and wind mass flux, should not change our modeling or qualitative conclusions. Following Equation (4), the jet velocity, which determines the specific energy of the jet, depends only on η and $\kappa_{\rm cho}$. Moreover, from K.-Y. Su et al. (2025b), we also conclude that under similar settings, feedback models self-regulate to a similar average AGN feedback energy $\langle \dot{E}_{\rm wind} \rangle$ (see also K.-Y. Su et al. 2023, 2025a), and the implied black hole accretion rate $\langle \dot{m}_{\rm BH} \rangle \sim \langle \dot{E}_{\rm wind} \rangle / \eta c^2$ depends only on the feedback efficiency η. If anything, if the overall Bondi accretion rate is further lowered by a factor of a few following the adiabatic expression, the black hole accretion rate may be reduced even more, making the dilemma in Section 4.1 slightly more severe.

A.3. AGN Wind Implementation

We implement AGN wind launching using a particle spawning method (P. Torrey et al. 2020; K.-Y. Su et al. 2021; R. Weinberger et al. 2023; K.-Y. Su et al. 2024), which injects new gas resolution elements directly from the central black hole. This method offers improved control over jet properties, as it reduces sensitivity to neighbor-finding routines and allows us to enforce higher resolution for the launched material. The feedback setup used here is similar to that in P. Torrey et al. (2020), which explored the impact of broad absorption line winds on disk galaxies.

The mass resolution of spawned gas particles is listed in Table 1, and they are prevented from derefining (i.e., merging into standard gas elements) until their velocity drops below 10% of the launch speed. To conserve linear momentum exactly, we inject two particles simultaneously in opposite directions whenever the accumulated jet mass flux equals twice the target mass per particle.

Each wind particle is initialized at a random point on a sphere of radius r_0, defined as either 50 comoving pc h^{-1} or half the black hole–nearest-gas-particle separation, whichever is smaller. The initial velocity vector is radial. The magnetic field of the launched particle is initialized to $<10^{-4}$ G in the z-direction, and the initial gas temperature is set to 10^7 K. Both magnetic and thermal energy fluxes are subdominant compared to the kinetic energy flux of the wind.

A.4. Initial Conditions

The initial conditions consist of a 100 comoving Mpc h^{-1} box with a zoom-in region centered on a halo that reaches $\sim 10^{14} M_\odot$ at $z = 0$. Within the zoom-in region, the dark-matter particle mass is $8.4 \times 10^6 M_\odot h^{-1}$, and the initial gas mass resolution is $1.6 \times 10^6 M_\odot h^{-1}$. The initial seeded magnetic field is set to 10^{-10} G. The run was first evolved without black holes to $z = 7.2$ for the early seed case, or to $z = 4.5$ for all other runs listed in Table 1, at which point the simulations were restarted with black holes and AGN feedback, corresponding to the earliest seeding time implied by each black hole seeding model.

Once a black hole is seeded, we enable on-the-fly super-Lagrangian hyperrefinement of gas particles, achieving a maximum resolution of $4 \times 10^5 M_\odot h^{-1}$ within 15 comoving kpc h^{-1} of the black hole. All runs are evolved to $z = 1$ (and not $z = 0$, because of computational cost); by this epoch, the principal differences among models are already apparent. A full evolution to $z = 0$ is deferred to future work.

Appendix B
Possible Future Improvements and Current Limitations

B.1. Geometrical Effects and Efficiency of the AGN Feedback

Although H. Cho et al. (2025) obtain an AGN jet for the nonzero black hole spin case, we launch an isotropic wind in this study for simplicity; this is a key limitation of the present study. At our resolution, geometric effects of AGN feedback may be subdominant. Moreover, in the higher specific-energy cases ($\eta \gtrsim 0.3$), which correspond to higher black hole spins, the initially elongated jet cocoon tends to isotropize and evolve into a quasi-spherical bubble on small scales, even when it is adequately resolved (K.-Y. Su et al. 2021, 2024).

However, an initially more collimated jet may still be less efficient at regulating the cooling flow and quenching star formation and black hole growth (K.-Y. Su et al. 2021, 2024). Meanwhile, a more collimated feedback may sustain steadier black hole accretion while transporting energy to larger radii. The impact of such geometric effects and a detailed modeling of the angular dependence of wind mass, kinetic, and thermal energy fluxes are left to future exploration.

B.2. Resolution Effect

The gas mass resolution in this study is $\sim 4 \times 10^5 M_\odot$, which is sufficient to ensure convergence for SNe feedback (P. F. Hopkins et al. 2018b) and a good behavior for FIRE stellar feedback models (e.g., R. Feldmann et al. 2017). However, it is lower than that in our previous isolated galaxy simulations (K.-Y. Su et al. 2025b), due to the higher computational cost of cosmological zoom-in runs.

The implications for black hole accretion and AGN feedback remain broadly consistent with the discussion in K.-Y. Su et al. (2025b). The dominant uncertainties still lie in the estimation of the accretion rate, rather than in the feedback injection process. The resolution of the spawned wind particles differs by only a factor of $\sim$3.5 compared to our previous isolated runs. For the feedback injection itself, resolution effects are expected to become more significant in future work if we explicitly model the angular distribution of jet mass and energy fluxes.

Regarding black hole accretion, the Bondi radius is often unresolved in the vicinity of the black hole, particularly when the black hole mass is still relatively low. Nevertheless, we estimate the Bondi accretion rate and the suppression prefactor ($\kappa_{\rm Cho}$) using kernel-weighted averages of gas density and temperature within a smoothing radius, without applying any rescaling despite the radius of the kernel. This choice is motivated by the multizone GRMHD simulations of H. Cho et al. (2024), which include realistic galactic potentials and gas profiles, and demonstrate that the density and temperature remain relatively flat over the range 10^5–10^8 r_g (corresponding to $\sim$30 pc–3 kpc). We therefore assume that the values measured in our simulations are representative of those at the Bondi radius, had it been resolved.

Given this, we do not expect our resolution to qualitatively bias the overall black hole accretion rate. However, we acknowledge that limited resolution may introduce scatter in the accretion rate over time. A more detailed examination of these effects is deferred to future work.

B.3. Black Hole Positioning and Mergers

At the current resolution, it is not possible to accurately capture the dynamical friction required to sink the black hole to the potential minimum. We therefore adopt the approach of S. Wellons et al. (2023), in which the black hole identifies the most deeply bound particle and is repositioned continuously with a velocity-damping term. This combination yields the most stable centering behavior in practice. However, this subgrid repositioning scheme may affect the black hole merger rate, and its impact will be explored in future studies with higher resolution.

ORCID iDs

Kung-Yi Su https://orcid.org/0000-0003-1598-0083
Angelo Ricarte https://orcid.org/0000-0001-5287-0452
Priyamvada Natarajan https://orcid.org/0000-0002-5554-8896
Antonio J. Porras-Valverde https://orcid.org/0000-0002-1996-0445
Hyerin Cho (혜린조) https://orcid.org/0000-0002-2858-9481
Ramesh Narayan https://orcid.org/0000-0002-1919-2730
Claude-André Faucher-Giguère https://orcid.org/0000-0002-4900-6628
Philip F. Hopkins https://orcid.org/0000-0003-3729-1684
Ben S. Prather https://orcid.org/0000-0002-0393-7734

References

Anglés-Alcázar, D., Davé, R., Faucher-Giguère, C.-A., Özel, F., & Hopkins, P. F. 2017a, MNRAS, 464, 2840
Anglés-Alcázar, D., Faucher-Giguère, C.-A., Quataert, E., et al. 2017b, MNRAS, 472, L109
Anglés-Alcázar, D., Quataert, E., Hopkins, P. F., et al. 2021, ApJ, 917, 53
Baldry, I. K., Glazebrook, K., Brinkmann, J., et al. 2004, ApJ, 600, 681
Behroozi, P. S., Conroy, C., & Wechsler, R. H. 2010, ApJ, 717, 379
Bell, E. F., McIntosh, D. H., Katz, N., & Weinberg, M. D. 2003, ApJS, 149, 289
Bhowmick, A. K., Blecha, L., Kelley, L. Z., et al. 2025, ApJ, 991, 81
Bhowmick, A. K., Blecha, L., Torrey, P., et al. 2024, MNRAS, 531, 4311
Bhowmick, A. K., Blecha, L., Torrey, P., et al. 2026, ApJ, 997, 187
Blanton, M. R., Eisenstein, D., Hogg, D. W., Schlegel, D. J., & Brinkmann, J. 2005, ApJ, 629, 143
Byrne, L., Faucher-Giguère, C.-A., Stern, J., et al. 2023, MNRAS, 520, 722
Byrne, L., Faucher-Giguère, C.-A., Wellons, S., et al. 2024, ApJ, 973, 149
Chatterjee, K., Chael, A., Tiede, P., et al. 2023, Galax, 11, 38
Cho, H., & Narayan, R. 2025, ApJ, 991, 89
Cho, H., Prather, B. S., Narayan, R., Su, K.-Y., & Natarajan, P. 2025, ApJ, 995, 122
Cho, H., Prather, B. S., Narayan, R., et al. 2023, ApJL, 959, L22
Cho, H., Prather, B. S., Su, K.-Y., Narayan, R., & Natarajan, P. 2024, ApJ, 977, 200
Dekel, A., & Birnboim, Y. 2006, MNRAS, 368, 2
Event Horizon Telescope Collaboration, Akiyama, K., Alberdi, A., et al. 2022, ApJL, 930, L16
Event Horizon Telescope Collaboration, Akiyama, K., Algaba, J. C., et al. 2021, ApJL, 910, L13
Fabian, A. C., Arnaud, K. A., Bautz, M. W., & Tawara, Y. 1994, ApJL, 436, L63
Faucher-Giguère, C.-A., Lidz, A., Zaldarriaga, M., & Hernquist, L. 2009, ApJ, 703, 1416
Feldmann, R., & Mayer, L. 2015, MNRAS, 446, 1939
Feldmann, R., Quataert, E., Hopkins, P. F., Faucher-Giguère, C.-A., & Kereš, D. 2017, MNRAS, 470, 1050
Fiacconi, D., Sijacki, D., & Pringle, J. E. 2018, MNRAS, 477, 3807
Gammie, C. F., McKinney, J. C., & Tóth, G. 2003, ApJ, 589, 444
Gaspari, M., Ruszkowski, M., & Oh, S. P. 2013, MNRAS, 432, 3401
Gorski, M. D., & Murchikova, E. 2025, arXiv:2509.10615
Guo, M., Stone, J. M., Kim, C.-G., & Quataert, E. 2023, ApJ, 946, 26
Guo, M., Stone, J. M., Quataert, E., & Kim, C.-G. 2024, ApJ, 973, 141
Guo, M., Stone, J. M., Quataert, E., & Springel, V. 2025, ApJ, 987, 202
Hopkins, P. F. 2015, MNRAS, 450, 53
Hopkins, P. F. 2016, MNRAS, 462, 576
Hopkins, P. F., Hernquist, L., Cox, T. J., et al. 2006a, ApJS, 163, 1
Hopkins, P. F., Narayan, R., & Hernquist, L. 2006b, ApJ, 643, 641
Hopkins, P. F., & Most, E. R. 2025, arXiv:2510.09756
Hopkins, P. F., Narayanan, D., & Murray, N. 2013, MNRAS, 432, 2647
Hopkins, P. F., & Quataert, E. 2010, MNRAS, 407, 1529
Hopkins, P. F., & Raives, M. J. 2016, MNRAS, 455, 51
Hopkins, P. F., Wetzel, A., Kereš, D., et al. 2018a, MNRAS, 480, 800
Hopkins, P. F., Wetzel, A., Kereš, D., et al. 2018b, MNRAS, 477, 1578
Hopkins, P. F., Grudic, M. Y., Su, K.-Y., et al. 2024, OJAp, 7E, 18
Kaaz, N., Liska, M., Tchekhovskoy, A., Hopkins, P. F., & Jacquemin-Ide, J. 2025, ApJ, 979, 248
Kauffmann, G., Heckman, T. M., White, S. D. M., et al. 2003, MNRAS, 341, 54
Kereš, D., Katz, N., Davé, R., Fardal, M., & Weinberg, D. H. 2009, MNRAS, 396, 2332
Kereš, D., Katz, N., Weinberg, D. H., & Davé, R. 2005, MNRAS, 363, 2
Kroupa, P. 2002, Sci, 295, 82
Kroupa, P., Subr, L., Jerabkova, T., & Wang, L. 2020, MNRAS, 498, 5652
Lalakos, A., Gottlieb, O., Kaaz, N., et al. 2022, ApJL, 936, L5
Leitherer, C., Schaerer, D., Goldader, J. D., et al. 1999, ApJS, 123, 3
Li, Y., & Bryan, G. L. 2014, ApJ, 789, 153
Madgwick, D. S., Somerville, R., Lahav, O., & Ellis, R. 2003, MNRAS, 343, 871
McDonald, M., Bayliss, M., Benson, B. A., et al. 2012, Natur, 488, 349
McDonald, M., Veilleux, S., & Mushotzky, R. 2011, ApJ, 731, 33
Mercedes-Feliz, J., Anglés-Alcázar, D., Hayward, C. C., et al. 2023, MNRAS, 524, 3446
Ni, Y., Di Matteo, T., Bird, S., et al. 2022, MNRAS, 513, 670
O'Dea, C. P., Baum, S. A., Privon, G., et al. 2008, ApJ, 681, 1035
Peterson, J. R., & Fabian, A. C. 2006, PhR, 427, 1
Porras–Valverde, A. J., Natarajan, P., Ricarte, A., et al. 2025a, arXiv:2511.08683
Porras-Valverde, A. J., Ricarte, A., Natarajan, P., et al. 2025b, arXiv:2504.11566
Porth, O., Chatterjee, K., Narayan, R., et al. 2019, ApJS, 243, 26
Pozzetti, L., Bolzonella, M., Zucca, E., et al. 2010, A&A, 523, A13
Rafferty, D. A., McNamara, B. R., & Nulsen, P. E. J. 2008, ApJ, 687, 899
Ressler, S. M., White, C. J., Quataert, E., & Stone, J. M. 2020, ApJL, 896, L6
Ricarte, A., Natarajan, P., Narayan, R., & Palumbo, D. C. M. 2025, ApJ, 980, 136
Ricarte, A., Tremmel, M., Natarajan, P., & Quinn, T. 2019, MNRAS, 489, 802
Rosas-Guevara, Y., Bower, R. G., Schaye, J., et al. 2016, MNRAS, 462, 190
Sijacki, D., Vogelsberger, M., Genel, S., et al. 2015, MNRAS, 452, 575
Springel, V., White, S. D. M., Tormen, G., & Kauffmann, G. 2001, MNRAS, 328, 726
Stern, J., Fielding, D., Faucher-Giguère, C.-A., & Quataert, E. 2019, MNRAS, 488, 2549
Su, K.-Y., Bryan, G. L., & Haiman, Z. 2025a, MNRAS, 538, 11
Su, K.-Y., Natarajan, P., Cho, H., et al. 2025b, ApJL, 981, L33
Su, K.-Y., Bryan, G. L., Haiman, Z., et al. 2023, MNRAS, 520, 4258
Su, K.-Y., Bryan, G. L., Hayward, C. C., et al. 2024, MNRAS, 532, 2724
Su, K.-Y., Hopkins, P. F., Bryan, G. L., et al. 2021, MNRAS, 507, 175
Su, K.-Y., Hopkins, P. F., Hayward, C. C., et al. 2019, MNRAS, 487, 4393
Talbot, R. Y., Bourne, M. A., & Sijacki, D. 2021, MNRAS, 504, 3619
Tamura, T., Kaastra, J. S., Peterson, J. R., et al. 2001, A&A, 365, L87
Tchekhovskoy, A., Narayan, R., & McKinney, J. C. 2011, MNRAS, 418, L79
Torrey, P., Hopkins, P. F., Faucher-Giguère, C.-A., et al. 2020, MNRAS, 497, 5292
Voit, G. M., Donahue, M., Bryan, G. L., & McDonald, M. 2015, Natur, 519, 203
Weinberger, R., Springel, V., Pakmor, R., et al. 2018, MNRAS, 479, 4056
Weinberger, R., Su, K.-Y., Ehlert, K., et al. 2023, MNRAS, 523, 1104
Wellons, S., Faucher-Giguère, C.-A., Hopkins, P. F., et al. 2023, MNRAS, 520, 5394
Werner, N., Oonk, J. B. R., Canning, R. E. A., et al. 2013, ApJ, 767, 153
Wetzel, A. R., Tinker, J. L., & Conroy, C. 2012, MNRAS, 424, 232